Elsevier Editorial System(tm) for Earth and Planetary Science Letters
Manuscript Draft

Manuscript Number: EPSL-D-20-00655R2

Title: Global variations of Earth's 520- and 560-km discontinuities

Article Type: Letters

Keywords: 520-km discontinuity; 560-km discontinuity; SS precursors; mantle transition zone; mantle phase transformations; oceanic crust recycling

Corresponding Author: Dr. Dongdong Tian, Ph.D.

Corresponding Author's Institution: Michigan State University

First Author: Dongdong Tian, Ph.D.

Order of Authors: Dongdong Tian, Ph.D.; Mingda Lv; Songqiao S Wei, Ph.D.; Susannah M Dorfman, Ph.D.; Peter M Shearer, Ph.D.

Abstract: We investigate seismic discontinuities in the mantle transition zone (MTZ) by analyzing SS precursors recorded at global seismic stations. Our observations confirm the global existence of the 520-km discontinuity. Although substantial regional depth variations in the 520-km discontinuity are generally correlated with temperature in the mid-MTZ, they cannot be fully explained by the Clapeyron slope of the wadsleyite-ringwoodite phase transition, suggesting both thermal and compositional heterogeneities in the MTZ. A second discontinuity at ~560-km depth, previously interpreted as splitting of the 520-km discontinuity, is most commonly detected in cold subduction zones and hot mantle regions. The depth separation between the 520- and 560-km discontinuities varies from ~80 km in cold regions to ~40 km in hot areas. The exsolution of calcium-perovskite (Ca-pv) from majorite garnet has been proposed to explain the velocity and density changes across the 560-km discontinuity. However, the gradual exsolution of perovskite and partitioning of Ca and Al between perovskite and garnet appear inconsistent with the relatively "sharp" discontinuity in seismic observations and thus need to be revisited in the future. Nevertheless, because the only known transition in major minerals at this depth in the MTZ is the formation of Ca-pv, the existence of the 560-km discontinuity may imply localized high calcium concentrations in the mid-MTZ possibly related to the recycling of oceanic crust.

Responses to Editor's Comments
(Manuscript EPSL-D-20-00655R1)

The collection of Figures in the Supplementary Material has insufficient explanation, e.g., there is no discussion at all of what is supposed to be learnt from the discontinuity topography examples in Figure S4. Acceptance is conditional on the provision of Text explaining all of the Supplementary Figures. Also make sure that all labelling can actually be read.

We appreciate the editor's comments on the Supplementary Material. We have added several sections in the Supplementary Texts to explain the Supplementary Figures that are not well explained in the main text. We have also improved the legibility of the figures and their captions. We hope the new version will prove satisfactory.

Global variations of Earth's 520- and 560-km discontinuities

Dongdong Tian*, Mingda Lv, S. Shawn Wei, Susannah M. Dorfman, Peter M. Shearer

Corresponding author: Dongdong Tian (tiandong@msu.edu)

Highlights

1. We map the global distribution of the 520-km discontinuity.
2. Depth variations of the 520-km discontinuity correlate with the mid-MTZ temperature.
3. Compositional heterogeneity also contributes to the 520-km discontinuity topography.
4. A 560-km discontinuity is sporadically detected in subduction zones and mantle upwells.
5. The 560-km discontinuity implies localized Ca-enrichment due to recycled oceanic crust.

Global variations of Earth's 520- and 560-km discontinuities

Dongdong Tian[1*], Mingda Lv[1], S. Shawn Wei[1], Susannah M. Dorfman[1], Peter M. Shearer[2]

1. Department of Earth and Environmental Sciences, Michigan State University, East Lansing, MI 48824, USA
2. Institute of Geophysics and Planetary Physics, Scripps Institution of Oceanography, University of California, San Diego, La Jolla, CA 92037, USA

*Corresponding author: Dongdong Tian (tiandong@msu.edu)

Abstract

We investigate seismic discontinuities in the mantle transition zone (MTZ) by analyzing SS precursors recorded at global seismic stations. Our observations confirm the global existence of the 520-km discontinuity. Although substantial regional depth variations in the 520-km discontinuity are generally correlated with temperature in the mid-MTZ, they cannot be fully explained by the Clapeyron slope of the wadsleyite-ringwoodite phase transition, suggesting both thermal and compositional heterogeneities in the MTZ. A second discontinuity at ~560-km depth, previously interpreted as splitting of the 520-km discontinuity, is most commonly detected in cold subduction zones and hot mantle regions. The depth separation between the 520- and 560-km discontinuities varies from ~80 km in cold regions to ~40 km in hot areas. The exsolution of calcium-perovskite (Ca-pv) from majorite garnet has been proposed to explain the velocity and density changes across the 560-km discontinuity. However, the gradual exsolution of perovskite and partitioning of Ca and Al between perovskite and garnet appear inconsistent with the relatively "sharp" discontinuity in seismic observations and thus need to be revisited in the future.

Nevertheless, because the only known transition in major minerals at this depth in the MTZ is the formation of Ca-pv, the existence of the 560-km discontinuity may imply localized high calcium concentrations in the mid-MTZ possibly related to the recycling of oceanic crust.

Keywords

520-km discontinuity; 560-km discontinuity; SS precursors; mantle transition zone; mantle phase transformations; oceanic crust recycling

1 Introduction

Seismic discontinuities in the mantle provide critical insight into thermal and compositional states of Earth's mantle and its dynamics. Two major seismic discontinuities at depths of approximately 410 km and 660 km mark the top and bottom of the mantle transition zone (MTZ). These discontinuities are observed globally by different seismic techniques (e.g., Deuss et al., 2013) and are prominent in 1D reference Earth models (e.g., Kennett et al., 1995). The discontinuities are generally linked to phase transformations in the olivine system. Their depths, topography, and sharpness are sensitive to thermal and compositional heterogeneities in the MTZ. Olivine transforms to wadsleyite at ~410 km depth, with a positive Clapeyron slope, whereas ringwoodite transforms to bridgmanite and ferropericlase at ~660 km depth, with a negative Clapeyron slope (Akaogi et al., 1989; Ito & Takahashi, 1989; Katsura & Ito, 1989). These opposite Clapeyron slopes result in an elevated 410-km discontinuity and a depressed 660-km discontinuity in cold regions, and vice versa, making the MTZ thickness a robust thermometer of the upper mantle (e.g., Helffrich, 2000).

In addition to the phase changes near 410- and 660-km depth, the transformation of wadsleyite to ringwoodite is expected to take place in the MTZ, resulting in a discontinuity at ~520 km depth (Rigden et al., 1991). The Clapeyron slope of this phase transition is positive and larger than that of the olivine-wadsleyite transition (Helffrich, 2000). Therefore, we expect both the 410- and 520-km discontinuities to be elevated and a smaller separation between them in cold regions. Mineralogical experiments show that the wadsleyite-ringwoodite phase transition has a smaller impedance contrast and occurs over a wider depth/pressure interval compared to the 410- and 660-km discontinuities (Rigden et al., 1991). Consequently, the 520-km discontinuity is relatively weaker and more challenging to detect.

The weak and ambiguous observations of the 520-km discontinuity using a variety of seismological methods have fueled ongoing debates about its global distribution and variations. The discontinuity was first observed as an abrupt change in velocity gradient from P wave reflection data (e.g., Hoffman et al., 1961), although its existence was questioned by later studies using the same type of data (e.g., Cummins et al., 1992). Unambiguous observations of the 520-km discontinuity were obtained with large volumes of digital seismic data in the 1990s, suggesting a global discontinuity with an impedance contrast of ~3%, roughly half of the impedance contrasts for the 410- and 660-km discontinuities, and a transition interval no thicker than 50 km (Shearer, 1990, 1991, 1996). The seismic signals of the 520-km discontinuity are observed in different seismic data types, e.g., SS and PP precursors, ScS reverberations, receiver functions, P’P’ precursors, and P wave triplications (see Fig. 1a for a summary map of previous observations). Debates continue regarding the global existence of the 520-km discontinuity.

Shearer (1990, 1991) provided the first evidence for its global characteristics by stacking long-period seismic data. In contrast, with a similar technique and global dataset, Gu et al. (1998) observed the 520-km discontinuity only beneath oceans but not under continental shields, whereas Deuss and Woodhouse (2001) found the 520-km discontinuity in most regions (both continental and oceanic) with a few exceptions. Global and regional receiver function studies usually found it a regionally intermittent discontinuity (e.g., Chevrot et al., 1999; Lawrence & Shearer, 2006), while short-period P'P' precursor studies generally could not detect signals related to the discontinuity (e.g., Benz & Vidale, 1993).

More intriguingly, another weaker discontinuity beneath the 520-km discontinuity is sporadically observed in the MTZ, initially termed splitting of the 520-km discontinuity. Using long-period SS precursor data, Deuss and Woodhouse (2001) observed double discontinuities at about 500- and 560-km depths beneath the Indonesian subduction zone and North America shield. The second and weaker discontinuity at ~560 km depth (hereafter as the 560-km discontinuity) is only intermittently observed in SS and PP precursors, ScS reverberations, and receiver functions (see Fig. 1b for a summary map of previous observations).

The only phase transition observed to take place at equilibrium conditions corresponding to ~560 km depth in any major phase in bulk compositions ranging from harzburgite to mid-ocean ridge basalt (MORB) is the garnet to Ca-perovskite (Ca-pv) transition. As a result, explanations for the 560-km discontinuity focus on the garnet-Ca-pv transition. Deuss and Woodhouse (2001) proposed that at an average mantle temperature of 1500 K, the wadsleyite-ringwoodite and garnet-Ca-perovskite transitions occur at the same depth, resulting in a single discontinuity at

~520 km. When temperature changes, the two phase transitions separate, leading to the observed double discontinuities at about 500 km and 560 km. However, this explanation was challenged by later laboratory experiments (Saikia et al., 2008), which reported a positive Clapeyron slope for the garnet-Ca-pv transition. Saikia et al. (2008) further proposed that regional variations of the 560-km discontinuity are controlled by compositional heterogeneities (i.e., Ca concentration in the mid-MTZ) rather than thermal heterogeneities. In Ca-poor regions, the garnet-Ca-pv transition is negligible, and only the 520-km discontinuity can be observed. In contrast, in Ca-rich regions both the 520- and 560-km discontinuities are observable.

Detailed observations of the 520- and 560-km discontinuities can help us better constrain the temperature and composition of the mid-MTZ. However, due to limited data, the global distribution and variations of the two discontinuities have not been well mapped. With the deployment of numerous broadband seismic stations during the last two decades, more high-quality data are publicly available. In this study, we investigate global variations of both the 520- and 560-km discontinuities with the largest compilation of SS precursor data published to date and discuss the implications for the thermal state, composition, and dynamics of Earth's upper mantle.

2 Data and Methods

2.1 Data processing

We analyze long-period SS precursors to study the detailed structure of the upper mantle discontinuities. SS is a shear wave reflected at the surface, while SS precursors (termed S*d*S) are underside reflections off the *d*-km discontinuity (Fig. 2a). SS precursors sample the upper mantle at the midpoints between sources and receivers, providing good data coverage on both continents and oceans.

We use broadband seismic waveform data recorded by all global permanent stations during 1970–2018 available at the Incorporated Research Institutions for Seismology (IRIS) Data Management Center, USArray Transportable Array (TA) stations during 2004–2018, and F-net stations in Japan during 1995–2018 (Fig. 2b). We select earthquakes shallower than 75 km to reduce interference from depth phases, and limit earthquake magnitudes to $5.5 \leq M \leq 7.0$ to ensure good signal-to-noise ratios (see Fig. 2b for the geographic distribution and Fig. S1 for the depth and magnitude histograms of earthquakes). This search yields more than 3.2 million records in a source-receiver distance range of 90°–180°. The seismograms are then converted to velocity records, rotated to transverse components, bandpass filtered at the periods of 15–75 s with a first-order, zero-phase Butterworth filter, and resampled to 1 Hz sampling rate.

For each record, the SS phase is automatically picked by searching for the maximum amplitude of the transverse component in a 60-s long time window centered at the predicted SS arrival time from the AK135 model (Kennett et al., 1995). The noise level is then estimated by measuring the maximum amplitude in a time window from 50 s before the predicted S*660*S arrival to 50 s after the predicted S*410*S arrival. Records with signal-to-noise ratios (SNR) of SS smaller than 3.0 are discarded. Each trace is then normalized by its SS phase maximum amplitude and aligned to the automatically determined SS peak. The polarity of each trace is flipped if necessary to make sure the SS peak amplitude is always larger than its negative sidelobes. To further remove some distorted SS waveforms, a global reference SS waveform is built by stacking all SS waveforms along their peaks with equal weighting, as SNR weighting has negligible effects on the global SS waveform. Records are discarded if cross-correlation coefficients (CCs) with the global reference SS waveform are smaller than 0.6, or if the absolute value of the negative coefficient is larger than the positive one. The CC threshold is determined empirically by manually checking the SS waveforms. We repeat these procedures iteratively to discard bad traces. Such data quality control criteria lead to ~265,000 records with good global coverage.

2.2 Waveform stacking

SS precursor signals are usually too weak to observe clearly on individual seismograms and stacking is required to enhance their visibility. To study lateral variations of the 520- and 560-km discontinuities, we divide the globe into 1654 overlapping circular caps with 5° spacing and 10° radius, and stack traces reflected in each cap. SS waveforms in a 160-s long time window are aligned and stacked along the automatically determined SS peaks. Because the slownesses of S*410*S, S*520*S, and S*660*S are slightly different, we stack waveforms of each phase in a 200-s long time window along the predicted traveltime curve for that phase from the AK135 model (Kennett et al., 1995). The three segments of S*410*S, S*520*S, and S*660*S are then truncated and non-overlappingly concatenated to produce the final S*d*S waveforms. The uncertainties of the stacked waveforms are estimated using a bootstrap resampling method (Efron & Tibshirani, 1991) by stacking waveforms of 300 random subsets of the dataset.

We exclude traces outside the source-receiver distance range of 110°–145° from stacking to minimize the contamination of interfering phases. Fig. 3 shows the stacks of the entire global dataset in 1°-wide bins of source-receiver distance. The main SS phase (red streak aligned at zero time) and its major precursors S*410*S and S*660*S are consistent with the predicted traveltime curves from the AK135 model (Kennett et al., 1995). Also clearly seen are Ss*660*s (topside reflection from the 660-km discontinuity) and ScS*660*ScS (underside reflection of core-reflected S wave from the 660-km discontinuity), which interfere with our target S*d*S phase, S*520*S and S*560*S, at the source-receiver distances of 105° and 153°, respectively. Since these strong interfering phases could bias the stacked S*d*S waveforms, we exclude traces outside the source-receiver distance range of 110°–145°, leading to ~140,000 records for the following analyses. The new limited dataset still provides good global coverage (Fig. 2c) with robust and unbiased results.

2.3 S*d*S phase detection

Major S*d*S phases, S*410*S and S*660*S, are usually prominent in the stacked S*d*S waveforms. Since S*d*S and SS share similar ray paths, their waveforms should be nearly identical despite their different amplitudes. We thus use the stacked SS phase as a reference and apply cross-correlation to detect these two phases automatically. Signals with stacking uncertainties higher than half of their peak amplitudes are considered unreliable and discarded.

On the other hand, minor S*d*S phases, e.g., potential S*520*S and S*560*S, usually have low amplitudes and are likely to be contaminated by sidelobes of S*410*S and S*660*S signals. Following Shearer (1996), we detect S*520*S and S*560*S by comparing them with synthetic waveforms. Synthetic seismograms are constructed by scaling, shifting, and stretching the SS reference waveform to fit the observed S*410*S and S*660*S pulses, assuming no discontinuities other than the 410- and 660-km discontinuities. S*d*S residual waveforms are calculated by subtracting synthetic waveforms from observations. Thus, the S*d*S residual waveforms carry information about minor discontinuities only and should minimize contamination from the sidelobes of S*410*S and S*660*S signals. Peaks with a lower bound of their 95% confidence level greater than 0 in the S*d*S residual waveforms are identified as potential S*d*S phases. Single S*d*S signals are identified in most caps, while double S*d*S signals also are found in several caps (Fig. 4). The single S*d*S signal is designated either S*520*S or S*560*S, depending on the traveltime differences relative to the predictions. These double S*d*S signals are named S*520*S and S*560*S, respectively, although their depths may vary.

As expected, more traces produce more robust stacked waveforms with smaller uncertainties, especially for weak signals. Normalized amplitudes of S*410*S and S*660*S phases exhibit Gaussian distributions (Fig. S2a-b) with a mean value of about 0.03, consistent with previous observations of global mean S*d*S/SS amplitude ratios (Shearer & Flanagan, 1999). The fluctuations of the S*410*S and S*660*S amplitudes may result from lateral variations of the impedance contrast and sharpness of the 410- and 660-km discontinuities. However, amplitudes and stacking uncertainties of both S*520*S and S*560*S observations exhibit a strong dependence on the number of stacked traces (Fig. S2c-f), implying that stacking results are biased to larger amplitudes and uncertainties when data are insufficient. The amplitudes and stacking uncertainties of S*520*S and S*560*S phases tend to be stable when the number of stacked traces exceeds about 1000. The mean normalized amplitudes are 0.007 for S*520*S and 0.004 for S*560*S, much smaller than that of S*410*S and S*660*S. In this study, stacked waveforms with less than 200 traces or stacking uncertainties greater than 0.004 are discarded to balance the data quality and global data coverage.

2.4 Mapping S*d*S traveltimes to discontinuity depths

Observed S*d*S traveltimes can be further converted to depths of discontinuities. Owing to the similar ray paths shared by SS and all S*d*S phases, their differential traveltimes are only sensitive to topography of the two discontinuities/surface and shear-wave velocity in between. To estimate the absolute depth of a *d*-km discontinuity, the effects of surface topography and shear-wave velocity structure above the *d*-km discontinuity must be carefully determined and corrected. The depth corrections can be as large as a few tens of kilometers and are highly dependent on the choice of the 3D upper-mantle velocity model, making it difficult to estimate the absolute discontinuity depth (Schmerr & Garnero, 2006). In contrast, the differential depth between two mantle discontinuities can be determined robustly from the differential traveltime of two S*d*S phases. For example, the differential traveltime S*410*S-S*660*S is only sensitive to the shear-wave velocity structure between the 410- and 660-km discontinuities, which is more consistent among different tomography models compared to the shear-wave velocity structure above 410-km depth. After correcting for 3D shear-wave velocity structure in the MTZ, the differential traveltime S*410*S-S*660*S can be converted to MTZ thickness (i.e., differential depth between the 410- and 660-km discontinuities). Such corrections are only a few kilometers, and different tomography models give similar corrections with small differences (1–2 km) in MTZ thickness (Schmerr & Garnero, 2006). To reduce the potential biases of corrections from different tomography models, we obtain the apparent discontinuity depths and differential depths between discontinuities by only correcting for the 3D shear-wave velocity structure in the MTZ based on the S40RTS model (Ritsema et al., 2011). The discontinuity depth uncertainties are estimated using a bootstrap method (Efron & Tibshirani, 1991) to resample 300 random subsets of the dataset.

3 Results

3.1 Detection of the 520- and 560-km discontinuities

Fig. 3 shows that the 520-km discontinuity is a coherent global feature. Between S*410*S and S*660*S, a weaker but prominent phase is visible in the source-receiver distance range of 105°–180° (Fig. 3), except near 153°, where the ScS*660*ScS phase interferes with SS precursors. This phase matches well with the predicted arrival time and slowness of S*520*S and is interpreted as the underside reflection off the 520-km discontinuity (Shearer, 1991, 1996).

Our global survey of S*520*S stacked in overlapping bouncepoint caps further confirms the global existence of the 520-km discontinuity. Our data provide good global coverage, particularly in the northern hemisphere (Fig. 2c). In regions with sufficient data sampling, S*520*S is always strong enough to be robustly detected, as indicated by the S*520*S/S*410*S amplitude ratios (Fig. 5a). The average S*520*S/S*410*S amplitude ratio is about 0.32 (Fig. 5b), suggesting that the 520-km discontinuity is much weaker than the 410-km discontinuity, with a smaller impedance contrast and/or a wider transition interval. The S*520*S/S*410*S amplitude ratios also show regional variations, which can be greater than 0.5 in some regions (e.g., the Indonesian subduction zone). There is no apparent correlation between the lateral changes in S*520*S/S*410*S amplitude ratios, differential depths, MTZ S-wave velocity, and tectonic types (Fig. S3). The varying amplitudes may be attributed to impedance contrasts and sharpness changes of the discontinuities, focusing or defocusing effects due to the discontinuity topography, and uneven sampling in different regions. Fig. S4 shows synthetic S*520*S waveforms with a variety of discontinuity topographies computed by Kirchhoff migration (Shearer et al., 1999). Depth perturbations appear to be the dominant factor controlling the S*520*S amplitude. The tests also suggest that the vertical resolution of SS precursors is about 30–50 km.

Regional stacked waveforms also show sporadic existence of the 560-km discontinuity (Fig. 5c). Two minor S*d*S phases are detected between S*410*S and S*660*S in some regions, especially beneath the subduction zones along the Circum-Pacific belt (example waveforms are shown in Fig. S5). Fig. 5c shows the observed S*560*S/S*410*S amplitude ratios, and zero indicates null detection of the 560-km discontinuity although the data sampling is sufficient. The mean S*560*S/S*410*S amplitude ratio is 0.22 (Fig. 5d), smaller than that of S*520*S/S*410*S, making it more difficult to detect the 560-km discontinuity. The amplitude ratios also show regional variations, with stronger amplitudes beneath the Middle East, Eastern Africa, and Southeast Asia, whereas weaker amplitudes beneath north and east of Hawaii (Fig. 5c).

3.2 Depth variations of the 520- and 560-km discontinuities

The 520- and 560-km discontinuities show significant topographic changes. Bootstrap analysis for the discontinuity depths shows that the mean depth uncertainties for the 520- and 560-km discontinuities are ~9 km, much larger than the ~2.5-km mean uncertainties for the stronger 410- and 660-km discontinuities (Fig. S6). As expected, the depth uncertainty depends on the number of stacked traces, with larger uncertainties for smaller numbers of stacked traces (Fig. S7). After excluding data with depth uncertainties greater than 10 km, the apparent peak-to-peak depth variations are 46, 67, 77, and 56 km for the 410-, 520-, 560-, and 660-km discontinuities, respectively (Fig. 6). Given that the depth uncertainties for the 520- and 560-km discontinuities are larger than that of the 410-km discontinuity by a few kilometers, it is reasonable to conclude that the topographic changes of the 520- and 560-km discontinuities are greater than that of the 410-km discontinuity by at least 10–20 km.

The significant depth variation of the 520-km discontinuity is further revealed by the differential depths between the 520- and 410-km discontinuities (*d*520-*d*410) and between the 660- and 520-km discontinuities (*d*660-*d*520). Both differential depths vary by about 60 km, much larger than the MTZ thickness variation of 40 km (Figs. 7a, 7c, 7e). The differential depth *d*520-*d*410 is usually smaller in subduction zones, North America, and northern South America, and larger beneath most oceanic regions and Central Asia (Fig. 7a). Note that the differential depth *d*660-*d*520 shows an opposite trend with similar patterns (Fig. 7c). On the other hand, the differential depth *d*520-*d*410 shows no correlation (CC = 0.19) with the average shear-wave velocity perturbations in the depth range of 410–520 km (Fig. 7g), whereas the differential depth *d*660-*d*520 shows a slightly positive correlation (CC = 0.37) with the average shear-wave velocity perturbations in the depth range of 520–660 km (Fig. 7h). Therefore, it is reasonable to conclude that the 520-km discontinuity has larger depth variations than the 410- and 660-km discontinuities.

Similarly, the 560-km discontinuity also has large depth variations, as revealed by the differential depths *d*560-*d*410 and *d*660-*d*560 (Figs. 7b and 7d). The differential depth *d*560-*d*520 varies from ~80 km in Circum-Pacific subduction zone regions to ~40 km in sporadic regions beneath the Pacific Ocean (Fig. 7f), and shows a weak positive correlation (CC = 0.37) with the average shear-wave velocity perturbations in the depth range of 520–560 km (Fig. 7l). The 560-km discontinuity has the largest peak-to-peak depth variations compared to other discontinuities (Fig. 6). Since the sporadic 560-km discontinuity exists at varying depths, the global stacks in Fig. 3 do not show a consistent S*560*S signal.

3.3 Effects of data processing parameters on our observations

We perform a series of tests to check the effects of filtering parameters on our observations (Fig. 8). In general, a higher cut-off period of the filter does not significantly change the stacked waveforms, whereas the lower cut-off period controls short-wavelength waveforms. Compared to the filter of 15–75 s used in this study, a shorter-period filter of 15–60 s results in slightly stronger S*520*S and S*560*S signals, but also produces stronger sidelobes in the reference SS waveform (Fig. 8a). As expected, a longer-period filter of 25–75 s produces smoother signals with phases merging, and the narrower frequency band leads to strong sidelobes in the reference SS waveform (Fig. 8d). Using a filter of 10–75 s produces noisier waveforms, leading to a ~35% reduction in the number of high-quality records. Therefore, we conclude that the filter of 15–75 s used in this study can best preserve strong signal amplitudes and suppress sidelobes.

The geometry of bouncepoint caps may also affect the stacking results. Most global and regional SS precursor studies divide the globe or study regions into circular caps of 10˚ radius and 10° spacing (e.g., Flanagan & Shearer, 1998) to match the ~1000-km-wide Fresnel zone of SS precursors (e.g., Neele et al., 1997). Some studies use a smaller cap of 5° radius with dense data sampling (e.g., Houser et al., 2008). Schmerr and Garnero (2006) experimented with different radii of 5°, 10°, and 20°, and found that their observations of the MTZ thickness were almost identical for different cap sizes. Here we also try caps of 5˚ radius and 2˚ spacing, and caps of 10˚ radius and 10˚ spacing. The results for these cap geometries are shown in Figs. S8–S10.

Smaller caps have higher spatial resolution but contain less data, thus the S*d*S signals are more likely contaminated by randomly scattered signals and are biased to larger amplitudes and higher uncertainties (Figs. S8–S9). Although the cap size and number of records in each cap vary, the observed patterns of the 520- and 560-km discontinuities and differential depths are very similar to that in Figs. 5 and 7. We thus focus on our preferred results with caps of 10˚ radius and 5˚ spacing for further discussions.

We also test and rule out the possibility that the observed S*560*S signals are caused by depth phases. Based on the AK135 model (Kennett et al., 1995), a 60-km deep earthquake can generate a depth phase sS*660*S with a similar traveltime to S*560*S, which may bias detections of the 560-km discontinuity. Several reasons convince us that the observed S*560*S signals indeed indicate a 560-km discontinuity: (1) Differential traveltimes between sS*660*S and S*660*S are different for earthquakes at different depths. Since the stacked waveforms include traces from earthquakes with a variety of depths, it is unlikely to coherently stack these depth phases arriving at different times. (2) Although we limit our dataset to earthquakes shallower than 75 km, most of the earthquakes are shallower than 40 km (Fig. S1). It is unlikely that earthquakes at about 60-km depth dominate the stacking results. (3) We further limit our dataset to earthquakes shallower than 40 km and perform the same analysis. As shown in Fig. S11, the S*560*S detection results are identical to those using earthquakes shallower than 75 km. Thus, we conclude that our S*560*S observations are not biased by depth phases.

4 Discussion

4.1 Comparison with previous observations

Our observations of the 520- and 560-km discontinuities are generally in agreement with previous studies, but also show some differences. As shown in Fig. 1, previous studies using different seismic techniques also observed the 520- and 560-km discontinuities either globally or regionally. Flanagan and Shearer (1998) and Deuss and Woodhouse (2001) reported the 520-km discontinuity in most regions using SS precursors, in agreement with our observations. Deuss et al. (2006) and Thomas and Billen (2009) used PP precursors to detect the 520-km discontinuity beneath Alaska, the Indian Ocean, the mid-West, and the southwest Pacific. Our results show additional detections of the 520-km discontinuity beneath New Mexico, the Bering Sea, Northeastern Australia, Western Europe, and South China. In addition to the 560-km discontinuity detected beneath the Indonesian subduction zone, North America, and North China using SS or PP precursors (Deuss et al., 2006; Deuss & Woodhouse, 2001; Thomas & Billen, 2009), we also find much broader regions of this discontinuity beneath Western Europe, Eastern Africa, and Eastern North Pacific. The new detections probably result from the much larger dataset used in our study. Alternatively, since Deuss and Woodhouse (2001) limited their data to the source-receiver range of 100°–160°, interfering phases at source-receiver distances of 105° and 150° might bias their stacking results. In our study, we have more data sampling globally and further limit the source-receiver distance range to 110°–145° to minimize the effects of interfering phases. Thus we expect more robust and uncontaminated results with smaller uncertainties for global surveys of the 520- and 560-km discontinuities.

In contrast to SS precursor studies that observe the 520-km discontinuity globally, receiver function studies usually report sporadic existence of this discontinuity. Chevrot et al. (1999) only detected the 520-km discontinuity beneath 5 of 82 global stations, and Lawrence and Shearer (2006) found only 40% of global stations with this discontinuity. Regional receiver function studies with dense seismic arrays also imaged the discontinuity beneath parts of the US (e.g., Maguire et al., 2018; Schmandt, 2012), while other studies at shorter periods (e.g., 1.0–50 s) did not find it in the same regions (Cao & Levander, 2010). In addition, Deuss et al. (2013) observed the 520- and 560-km discontinuities beneath Western Asia using both SS precursors and receiver functions. In most regions where the 520-km discontinuity was detected using receiver functions, we also observe the 520-km discontinuity (Figs. 1a and 5a). Africa is an exception due to the insufficient data coverage of SS precursors (Fig. 2c).

A few studies using ScS reverberations or receiver functions also reported detections of the 560-km discontinuity beneath the Kuriles and Ryukyu subduction zones, Northeastern China, and the Mediterranean region (Fig. 1b). Our SS precursor data confirm the existence of the 560-km discontinuity in these regions (Fig. 5c), except the Mediterranean region, where SS precursors have poor data coverage (Fig. 2c). A few recent receiver function studies suggest a negative seismic discontinuity at the base of the MTZ beneath the Northwestern Pacific and the western US (e.g., Tauzin et al., 2017), where we find positive 520- and 560-km discontinuities.

The discrepancies between these different studies can be explained by the following reasons. (1) Short-period data are not sensitive to discontinuities with a transition interval thicker than 10 km (Benz & Vidale, 1993). By contrast, laboratory experiments and thermodynamic calculations show that the wadsleyite-ringwoodite phase transition occurs over a depth interval of 20–50 km (Akaogi et al., 1989; Katsura & Ito, 1989). Thus, short-period P'P' precursors (~1 Hz) and receiver functions (e.g., 1–50 s) are not sensitive to such a gradual discontinuity, while longer-period receiver functions (e.g., 5–50 s), ScS reverberations (e.g., 15–100 s), SS and PP precursors (e.g., 10–75 s) can detect it. (2) Different seismic data types depend on different material properties. SS precursors are sensitive to both density and shear-wave velocity contrasts across the discontinuity while receiver functions are sensitive only to its velocity contrast (Deuss et al., 2013). Laboratory experiments show that the shear-wave impedance contrast between wadsleyite and ringwoodite is 3–4.5%, whereas the compressional- and shear-wave velocity contrasts are only 1% (Rigden et al., 1991). A discontinuity with a small velocity contrast but a large density contrast can be observed in SS precursors but appear invisible in receiver functions and P wave triplications. (3) Small-scale lateral variations of discontinuity depth may lead to destructive interference for short-period energy, while long-period data tend to average out the lateral variations.

4.2 Seismic waveform modeling experiments

To further constrain the seismic properties of the 520- and 560-km discontinuities, we compute synthetic seismograms for a series of 1-D seismic models and compare them with observations. The 1-D models are designed by adding two discontinuities with varying sharpness and impedance contrasts at 520- and 560-km depths to the AK135 model (Kennett et al., 1995). As SS precursors are sensitive to the impedance contrast, we assume the same contrast for both velocity and density in the models. Following Wei and Shearer (2017), we calculate synthetic seismograms n by convolving the reference SS waveform with discontinuity operators, which include reflection and transmission coefficients and geometric spreading. As the observed S*d*S waveforms vary among caps, we choose the waveform of cap #0765 (see Fig. 4a for its geographic location) as a representative reference for comparisons. The reference S*d*S waveform has both S*520*S and S*560*S signals, and their amplitudes are close to the observed mean values. The synthetic seismogram for the AK135 model (Kennett et al., 1995) can fit the observed S*410*S and S*660*S signals but cannot produce the observed peaks in between (the gray trace in Fig. 9b). The model with a single 520-km discontinuity can explain the observed single peak in most regions but cannot produce the two separate peaks (red trace in Fig. 9b). Only the models with two discontinuities in the mid-MTZ can produce the observed double peaks (black traces in Fig. 9b).

Due to the limited resolution of long-period SS precursors, it is difficult to distinguish a sharp discontinuity from a gradual discontinuity with a higher impedance contrast. We model synthetic waveforms with a series of impedance contrasts and sharpnesses of the 520- and 560-km discontinuities. Our waveform modeling results show a strong trade-off between impedance contrast and sharpness of the discontinuities. Higher impedance contrasts enhance the S*d*S signals, whereas more gradual discontinuities weaken them. To fit the reference S*d*S waveform, the impedance contrasts are 2.4% and 2.0%, respectively, if both discontinuities are 0-km thick. Meanwhile, the impedance contrasts can be as high as 4.4% and 3.8% if both discontinuities occur over 30-km depth intervals (black traces in Fig. 9b).

4.3 Mineralogical implications of the 520-km discontinuity

The observed depth variations of the 520-km discontinuity can be explained predominately by effects of temperature on equilibrium phase transition pressure from wadsleyite to ringwoodite, plus modifications to phase transition depth by compositional heterogeneities. The Clapeyron slope of the wadsleyite-ringwoodite transition is positive and larger than that of the olivine-wadsleyite transition (Akaogi et al., 1989; Katsura & Ito, 1989). In contrast, the Clapeyron slope of the phase transition from ringwoodite to bridgmanite and ferropericlase is negative (Ito & Takahashi, 1989). Thus, we expect an elevated 520-km discontinuity and a larger separation between the 660- and 520-km discontinuities in cold mantle regions, and the opposite in hot regions. This is consistent with the first-order observations of the differential depth *d*660-*d*520 shown in Fig. 7c. The MTZ thickness correlates with shear-wave velocity perturbations in the MTZ (Fig. 7i), suggesting that they both are controlled by temperature. Assuming that the Clapeyron slopes of the olivine phase transitions at the 410-, 520-, 660-km discontinuities are 3.1 MPa/K, 5.3 MPa/K, and –2.0 MPa/K (Helffrich, 2000), respectively, a 40-km peak-to-peak variation of the MTZ thickness implies a change of 275 K in temperature. Such a temperature variation can cause a 60-km peak-to-peak difference in the differential depth *d*660-*d*520, in a good agreement with our observations (Fig. 7c). However, this thermal change of 275 K can only cause a 17-km peak-to-peak variation in the differential depth *d*520-*d*410, much smaller than the observed variation of 60 km (Fig. 7a). Also note that the differential depths *d*520-*d*410 and *d*660-*d*520 exhibit significant regional variations beneath the mid-Pacific, where we observe small MTZ thickness variations (Figs. 7a, 7c, and 7e). The apparent topographic changes of the 520-km discontinuity are too large to be solely explained by the Clapeyron slope of the wadsleyite-ringwoodite transition, implying compositional heterogeneities in modifying the transition depth.

Heterogeneities in components such as water and iron may contribute to depth variations of the 520-km discontinuity. Wadsleyite and ringwoodite have high water solubility to store up to 3 wt% water (Kohlstedt et al., 1996), and inclusions in diamond have demonstrated that ~1 wt% water is present in at least some locations in Earth's mantle (Pearson et al., 2014). Electrical conductivity in the MTZ (e.g., Huang et al., 2005) and seismic observations of a low-velocity layer above the 410-km discontinuity (e.g., Wei & Shearer, 2017) also provide evidence for a hydrous MTZ. Under hydrous conditions, the wadsleyite-ringwoodite transition appears as a sharper discontinuity at a greater depth (Inoue et al., 2010; Tsujino et al., 2019), whereas the 410-km discontinuity is elevated (Wood, 1995). These changes may result in a greater differential depth *d*520-*d*410 in hydrous regions compared to a dry mantle. However, the differential depth *d*520-*d*410 appears to be smaller than usual beneath northern and western Pacific subduction zones where high water content is expected in the mantle (Fig. 7a). In contrast, we observe large *d*520-*d*410 values beneath Central Asia and mid-ocean ridges where the mantle is thought to be dry. Therefore, we conclude that water in the MTZ has limited effects on 520-km discontinuity topography. In addition, the phase diagram of $(Mg,Fe)_2SiO_4$ indicates the iron-rich wadsleyite-ringwoodite transition occurs in a larger depth range at a shallower depth than the iron-free system (Frost, 2003). Since Fe/(Fe+Mg) mol% in MORB is three times higher than that in pyrolite (a hypothetical rock with the chemical composition of the upper mantle that reaches equilibrium) (Xu et al., 2008), localized enrichment of MORB may increase Fe/(Fe+Mg) mol% in the bulk composition and produce a shallower 520-km discontinuity.

4.4 Mineralogical implications of the 560-km discontinuity

Exsolution of Ca-pv from garnet can explain the existence of the 560-km discontinuity, i.e., splitting of the 520-km discontinuity. The observed differential depth *d*560-*d*520 is ~80 km in cold subduction zones, and ~40 km in hot oceanic regions (Fig. 7f). This temperature-controlled trend is consistent with the dominant control on differential thickness being the steep Clapeyron slope of the wadsleyite-ringwoodite phase transition. In contrast, the garnet-Ca-pv transition potentially responsible for the 560-km discontinuity is less sensitive to temperature than composition, based on laboratory experiments by Saikia et al. (2008). Saikia et al. (2008) further proposed that this phase transition was only seismically visible in Ca-rich regions. Thus, the intermittent detection of the 560-km discontinuity may suggest variable Ca concentrations in the MTZ.

However, one critical problem remains, in that the gradual phase transition reported in laboratory experiments (Saikia et al., 2008) and equilibrium thermodynamic simulations (Stixrude & Lithgow-Bertelloni, 2011) cannot generate a "sharp" discontinuity to be detectable by SS precursors. We assume that the mantle composition is an equilibrium mixture of two end-members of mantle differentiation, basalt and harzburgite. Then we calculate shear-wave velocity and density profiles of an equilibrium assemblage along the basalt-harzburgite join (Xu et al., 2008) under adiabats with a variety of potential temperatures (Fig. 9a and Fig. S12) using HeFESTo (Stixrude & Lithgow-Bertelloni, 2011), and also create a seismic model with a 60-km-thick gradual 560-km discontinuity (red curve in Fig. 9a) as reported by Saikia et al. (2008). Neither model can produce an S*560*S signal (orange and red traces in Fig. 9b, and Fig. S12). This discrepancy implies that the garnet-Ca-pv transition may occur over a narrower pressure range than previously reported, and the partitioning of Ca and implied Ca concentration required in regions where the 560-km discontinuity is observed may have been previously overestimated.

To further investigate the effects of Ca concentration on the 560-km discontinuity, we perform non-equilibrium thermodynamic modeling for comparison with seismic observations. The elastic properties of each mineral at pressure and temperature conditions at 410–660 km depths are modeled using the formalism of Stixrude and Lithgow-Bertelloni (2005). We calculate the velocity and density of the rock assemblage as the Voigt-Reuss-Hill average of individual minerals along adiabats with a variety of potential temperatures (Stixrude & Lithgow-Bertelloni, 2011). The thermoelastic parameters of each mineral employed in these calculations are summarized in Table S3. We assume the MTZ composition to be pyrolite, which consists of wadsleyite/ringwoodite (57 mol%) and majorite garnet/Ca-pv (43 mol%) (Irifune et al., 2010). Mg-Fe solid solutions with a mol% ratio of 92:8 are considered in the systems of Mg_2SiO_4-Fe_2SiO_4 and $Mg_3Al_2Si_3O_{12}$-$Fe_3Al_2Si_3O_{12}$, respectively. Ca-pv is thought to constitute 7–10 mol% (Irifune et al., 2010) in pyrolite and up to 23–30 mol% in MORB (Ricolleau et al., 2010), and the gradual exsolution of Ca-pv from majorite garnet starts at a depth of about 550–570 km (Saikia et al., 2008). In order to test the role of Ca-pv on the velocity and density contrasts of the 560-km discontinuity, we vary the Ca-pv proportion 7–20 mol% in the non-equilibrium assemblage of ringwoodite, majorite garnet, and Ca-pv at depths > 550 km.

The thermodynamic models predict a 2.1% impedance contrast across the 520-km discontinuity due to the wadsleyite-ringwoodite phase transition (Fig. 10). This impedance contrast is strong enough to produce a seismically observable signal for most regions. At ~560 km, the impedance contrast positively correlates with the proportion of Ca-pv in the non-equilibrium assemblage, increasing from 1.1% to 3.7% for Ca-pv concentrations from 7 mol% to 20 mol% (Fig. 10). Temperature has little effect on the impedance contrasts of the transitions (Fig. S13). As the reference seismic observation requires at least 2.0% impedance contrast for the 560-km discontinuity (Fig. 9b), the 1.1% impedance contrast for a pyrolitic mantle with 7 mol% Ca-pv is too small to generate visible seismic signals, which would explain why the 560-km discontinuity cannot be observed globally. The Ca-pv concentration needs to be at least ~13 mol% to produce seismically observable signals (Figs. 9b and 10). A much higher Ca-pv concentration is necessary if the exsolution of Ca-pv from garnet occurs gradually over a larger depth interval.

The exact Ca-pv concentration is challenging to determine due to limited constraints on partitioning between garnet and perovskite at MTZ conditions. Assuming an upper limit of 20 mol% Ca-pv in localized regions which produces a 3.7% impedance contrast (Fig. 10), the depth interval of the phase transition needs to be no more than 30 km to explain the seismic observations (Fig. 9b). In contrast, laboratory experiments report gradual exsolution of Ca-pv over a pressure range that corresponds to a depth interval of ~60 km (Saikia et al., 2008), which fails to explain the seismic observations (red trace in Fig. 9b). Similar discrepancies between a gradual phase transition interval and a sharp seismic discontinuity also have been noted for the 410-km discontinuity. Several studies in the 1990s proposed possible mechanisms to resolve the discrepancy for the 410-km discontinuity. First, the olivine-wadsleyite transition can be highly non-linear with most of the transition occurring over a narrow depth interval, resulting in an effectively “sharp” discontinuity (Helffrich & Wood, 1996; Stixrude, 1997). Second, the transition interval is also significantly affected by chemical exchange with other nontransforming minerals, e.g. pyroxene and garnet (Stixrude, 1997). We suspect that similar mechanisms can be applied for the 560-km discontinuity. Effects of other Ca- and Al-bearing minor phases in the MTZ need to be investigated to reconcile the seismically "sharp" 560-km discontinuity and the gradual exsolution of Ca-pv.

4.5 Geodynamic implications for the sporadic 560-km discontinuity

The detections of the 560-km discontinuity suggest a higher Ca concentration than the normal mantle. Oceanic crust (i.e., MORB) contains up to 23–30 mol% Ca-pv, compared to 7–10 mol% Ca-pv in pyrolite (Irifune et al., 2010). Thus, the sporadic detections of the 560-km discontinuity may imply localized enrichment of oceanic crust due to the recycling of subducted oceanic crust through Earth's mantle.

In subduction zones, oceanic lithosphere is transported into the Earth's interior with subducting slabs. The overlying subducted oceanic crust may become buoyant near the depth of 660 km and accumulate at the base of the MTZ to form a garnetite layer (Irifune & Ringwood, 1993). The enrichment of oceanic crust in the mid-MTZ can explain the broad detection of the 560-km discontinuity beneath active or ancient subduction zones, e.g., around the Circum-Pacific regions, North America, the Indonesia subduction zone region, and the Middle East.

The basaltic oceanic crust may further sink in the base of the lower mantle and partially melt (Hirose et al., 1999). As evidenced by diamond inclusions (Walter et al., 2011) and geodynamical modeling (Li et al., 2014), oceanic crust can return from the lower mantle to the mid or upper mantle entrained by upwelling plumes (Hofmann & White, 1982). This upwelling process, potentially enriching Ca in the mid-MTZ beneath the eastern Pacific Ocean, might explain the 560-km discontinuity near the Hawaiian and Galápagos plumes. The 560-km discontinuity, on the other hand, is also observed beneath southern Africa and northeast of South America, where no active subducting slabs or plumes are reported. Hypothetical active or fossil plumes (Turunen et al., 2019; VanDecar et al., 1995) may be responsible for localized Ca-enrichment beneath these regions.

5 Conclusions

We conduct a global survey of the 520- and 560-km discontinuities by stacking a large dataset of SS precursors. Our results confirm that the 520-km discontinuity is a weak global discontinuity, whereas the 560-km discontinuity is only sporadically observed at varying depths in specific regions.

The differential depths *d*520-*d*410 and *d*660-*d*520 both show ~60-km peak-to-peak variations and the 520-km discontinuity shows larger depth variations compared to the 410- and 660-km discontinuities. The observed depth variations are generally correlated with shear-wave velocity and temperature in the MTZ. However, the Clapeyron slope of the wadsleyite-ringwoodite phase transition cannot fully explain the observed depth variations of the 520-km discontinuity, suggesting that compositional heterogeneities in the mid-MTZ also contribute to the depth variations.

The 560-km discontinuity is sporadically observed in both cold subduction zones and hot mantle upwelling regions. The depth separation between the 520- and 560-km discontinuities varies from ~80 km in cold regions to ~40 km in hot areas, suggesting that the garnet-Ca-pv transition is less sensitive to temperature than the wadsleyite-ringwoodite transition. Our seismic waveform modeling and thermodynamic modeling require >13 mol% Ca-pv in the mid-MTZ and a transition interval <30 km to match the seismic observations. The latter is in contrast to the broad depth interval (~60 km) of the Ca-pv exsolution in the laboratory experiments, invoking a more complicated phase transition due to non-linearity and other minor minerals. Furthermore, we propose that the sporadic 560-km discontinuity is linked to localized enrichment of oceanic crust due to the recycling of oceanic crust through Earth's mantle.

Acknowledgments

We thank the editor, Brian Kennett, and three anonymous reviewers for providing helpful comments to improve the manuscript. We also thank Jeroen Ritsema for constructive comments. Raw seismic data are available from Incorporated Research Institution for Seismology Data Management Center (IRIS DMC, https://ds.iris.edu/ds/nodes/dmc/) under network IDs AC, AE, AF, AI, AK, AT, AU, AV, BE, BL, BX, C, C1, CB, CD, CH, CM, CN, CT, CU, CZ, DK, DR, DW, EI, G, GB, GE, GT, HL, HT, IC, II, IP, IU, JP, KN, KO, KP, KR, KS, KZ, LX, MC, MI, MM, MM, MS, MX, MY, NA, ND, NJ, NO, NR, NU, OE, OV, PL, PM, PR, PS, RM, RV, S, SV, TA, TM, TR, TT, TW, UK, US, VE, WI, and WM, and broadband seismograph network F-net in Japan (https://doi.org/10.17598/nied.0005). SOD (Owens et al., 2004) was used to download data from IRIS DMC. The Generic Mapping Tools (Wessel et al., 2019) was used to create the figures. Seismic data analysis was supported in part through computational resources and services provided by the Institute for Cyber-Enabled Research at Michigan State University. This work was made possible by NSF grants OCE-1842989 to S.S.W, EAR-1664332 to S.M.D., and EAR-1620251 to P.M.S. D.T. and S.S.W. were also supported by the MSU Geological Sciences Endowment.

References

Akaogi, M., Ito, E., & Navrotsky, A. (1989). Olivine-modified spinel-spinel transitions in the system Mg2SiO4-Fe2SiO4: Calorimetric measurements, thermochemical calculation, and geophysical application. *Journal of Geophysical Research: Solid Earth, 94*(B11), 15671-15685. https://doi.org/10.1029/JB094iB11p15671

Benz, H. M., & Vidale, J. E. (1993). Sharpness of upper-mantle discontinuities determined from high-frequency reflections. *Nature, 365*, 147-150. https://doi.org/10.1038/365147a0

Bird, P. (2003). An updated digital model of plate boundaries. *Geochemistry, Geophysics, Geosystems, 4*(3). https://doi.org/10.1029/2001GC000252

Cao, A., & Levander, A. (2010). High-resolution transition zone structures of the Gorda Slab beneath the western United States: Implication for deep water subduction. *Journal of Geophysical Research: Solid Earth, 115*(B7). https://doi.org/10.1029/2009JB006876

Chevrot, S., Vinnik, L., & Montagner, J. P. (1999). Global-scale analysis of the mantle Pds phases. *Journal of Geophysical Research, 104*(B9), 20203-20219. https://doi.org/10.1029/1999jb900087

Cummins, P. R., Kennett, B. L. N., Bowman, J. R., & Bostock, M. G. (1992). The 520-km discontinuity. *Bulletin of the Seismological Society of America, 82*(1), 323-336.

Deuss, A., Andrews, J., & Day, E. (2013). Seismic observations of mantle discontinuities and their mineralogical and dynamical interpretation. *Physics and Chemistry of the Deep Earth*, 297-323.

Deuss, A., Redfern, S. A. T., Chambers, K., & Woodhouse, J. H. (2006). The nature of the 660-kilometer discontinuity in Earth's mantle from global seismic observations of PP precursors. *Science, 311*, 198-201. https://doi.org/10.1126/science.1120020

Deuss, A., & Woodhouse, J. (2001). Seismic observations of splitting of the mid-transition zone discontinuity in Earth's mantle. *Science, 294*, 354-357. https://doi.org/10.1126/science.1063524

Efron, B., & Tibshirani, R. (1991). Statistical data analysis in the computer age. *Science, 253*(5018), 390-395. https://doi.org/10.1126/science.253.5018.390

Flanagan, M. P., & Shearer, P. M. (1998). Global mapping of topography on transition zone velocity discontinuities by stacking SS precursors. *Journal of Geophysical Research, 103*(B2), 2673-2692. https://doi.org/10.1029/97jb03212

Frost, D. J. (2003). The structure and sharpness of $(Mg,Fe)_2SiO_4$ phase transformations in the transition zone. *Earth and Planetary Science Letters, 216*(3), 313-328. https://doi.org/10.1016/S0012-821x(03)00533-8

Gu, Y. J., Dziewonski, A. M., & Agee, C. B. (1998). Global de-correlation of the topography of transition zone discontinuities. *Earth and Planetary Science Letters, 157*(1-2), 57-67. https://doi.org/10.1016/S0012-821x(98)00027-2

Helffrich, G. R. (2000). Topography of the transition zone seismic discontinuities. *Reviews of Geophysics, 38*(1), 141-158. https://doi.org/10.1029/1999RG000060

Helffrich, G. R., & Wood, B. J. (1996). 410 km discontinuity sharpness and the form of the olivine α-β phase diagram: resolution of apparent seismic contradictions. *Geophysical Journal International, 126*(2), F7-F12. https://doi.org/10.1111/j.1365-246X.1996.tb05292.x

Hirose, K., Fei, Y. W., Ma, Y. Z., & Mao, H. K. (1999). The fate of subducted basaltic crust in the Earth's lower mantle. *Nature, 397*(6714), 53-56. https://doi.org/10.1038/16225

Hoffman, J. P., Berg, J. W., Jr., & Cook, K. L. (1961). Discontinuities in the earth's upper mantle as indicated by reflected seismic energy. *Bulletin of the Seismological Society of America, 51*(1), 17-27.

Hofmann, A. W., & White, W. M. (1982). Mantle plumes from ancient oceanic crust. *Earth and Planetary Science Letters, 57*(2), 421-436. https://doi.org/10.1016/0012-821x(82)90161-3

Houser, C., Masters, G., Flanagan, M., & Shearer, P. (2008). Determination and analysis of long-wavelength transition zone structure using SS precursors. *Geophysical Journal International, 174*(1), 178-194. https://doi.org/10.1111/j.1365-246X.2008.03719.x

Huang, X. G., Xu, Y. S., & Karato, S. I. (2005). Water content in the transition zone from electrical conductivity of wadsleyite and ringwoodite. *Nature, 434*, 746-749. https://doi.org/10.1038/nature03426

Inoue, T., Ueda, T., Tanimoto, Y., Yamada, A., & Irifune, T. (2010). The effect of water on the high-pressure phase boundaries in the system Mg2SiO4-Fe2SiO4. *Journal of Physics: Conference Series, 215*, 012101. https://doi.org/10.1088/1742-6596/215/1/012101

Irifune, T., & Ringwood, A. E. (1993). Phase transformations in subducted oceanic crust and buoyancy relationships at depths of 600-800 km in the mantle. *Earth and Planetary Science Letters, 117*(1-2), 101-110. https://doi.org/10.1016/0012-821x(93)90120-X

Irifune, T., Shinmei, T., McCammon, C. A., Miyajima, N., Rubie, D. C., & Frost, D. J. (2010). Iron partitioning and density changes of pyrolite in Earth's lower mantle. *Science, 327*, 193. https://doi.org/10.1126/science.1181443

Ito, E., & Takahashi, E. (1989). Postspinel transformations in the system Mg2SiO4-Fe2SiO4 and some geophysical implications. *Journal of Geophysical Research, 94*(B8), 10637-10646. https://doi.org/10.1029/JB094iB08p10637

Katsura, T., & Ito, E. (1989). The system Mg2SiO4-Fe2SiO4 at high pressures and temperatures: Precise determination of stabilities of olivine, modified spinel, and spinel. *Journal of Geophysical Research, 94*(B11), 15663-15670. https://doi.org/10.1029/JB094iB11p15663

Kennett, B. L. N., Engdahl, E. R., & Buland, R. (1995). Constraints on seismic velocities in the Earth from traveltimes. *Geophysical Journal International, 122*(1), 108-124. https://doi.org/10.1111/j.1365-246X.1995.tb03540.x

Kohlstedt, D. L., Keppler, H., & Rubie, D. C. (1996). Solubility of water in the α, β and γ phases of (Mg,Fe)2SiO4. *Contributions to Mineralogy and Petrology, 123*(4), 345-357. https://doi.org/10.1007/s004100050161

Lawrence, J. F., & Shearer, P. M. (2006). Constraining seismic velocity and density for the mantle transition zone with reflected and transmitted waveforms. *Geochemistry Geophysics Geosystems, 7*, Q10012. https://doi.org/10.1029/2006gc001339

Li, M., McNamara, A. K., & Garnero, E. J. (2014). Chemical complexity of hotspots caused by cycling oceanic crust through mantle reservoirs. *Nature Geoscience, 7*(5), 366-370. https://doi.org/10.1038/ngeo2120

Maguire, R., Ritsema, J., & Goes, S. (2018). Evidence of subduction-related thermal and compositional heterogeneity below the United States from transition zone receiver functions. *Geophysical Research Letters, 45*(17), 8913-8922. https://doi.org/10.1029/2018gl078378

Neele, F., deRegt, H., & VanDecar, J. (1997). Gross errors in upper-mantle discontinuity topography from underside reflection data. *Geophysical Journal International, 129*(1), 194-204. https://doi.org/10.1111/j.1365-246X.1997.tb00949.x

Owens, T. J., Crotwell, H. P., Groves, C., & Oliver-Paul, P. (2004). SOD: Standing order for data. *Seismological Research Letters, 75*(4), 515-520. https://doi.org/10.1785/gssrl.75.4.515-a

Pearson, D. G., Brenker, F. E., Nestola, F., McNeill, J., Nasdala, L., Hutchison, M. T., et al. (2014). Hydrous mantle transition zone indicated by ringwoodite included within diamond. *Nature, 507*, 221-224. https://doi.org/10.1038/nature13080

Ricolleau, A., Perrillat, J.-P., Fiquet, G., Daniel, I., Matas, J., Addad, A., et al. (2010). Phase relations and equation of state of a natural MORB: Implications for the density profile of subducted oceanic crust in the Earth's lower mantle. *Journal of Geophysical Research: Solid Earth, 115*(B8). https://doi.org/10.1029/2009JB006709

Rigden, S. M., Gwanmesia, G. D., Fitz Gerald, J. D., Jackson, I., & Liebermann, R. C. (1991). Spinel elasticity and seismic structure of the transition zone of the mantle. *Nature, 354*, 143-145. https://doi.org/10.1038/354143a0

Ritsema, J., Deuss, A., van Heijst, H. J., & Woodhouse, J. H. (2011). S40RTS: a degree-40 shear-velocity model for the mantle from new Rayleigh wave dispersion, teleseismic traveltime and normal-mode splitting function measurements. *Geophysical Journal International, 184*(3), 1223-1236. https://doi.org/10.1111/j.1365-246X.2010.04884.x

Saikia, A., Frost, D. J., & Rubie, D. C. (2008). Splitting of the 520-kilometer seismic discontinuity and chemical heterogeneity in the mantle. *Science, 319*, 1515-1518. https://doi.org/10.1126/science.1152818

Schmandt, B. (2012). Mantle transition zone shear velocity gradients beneath USArray. *Earth and Planetary Science Letters, 355*, 119-130. https://doi.org/10.1016/j.epsl.2012.08.031

Schmerr, N., & Garnero, E. (2006). Investigation of upper mantle discontinuity structure beneath the central Pacific using SS precursors. *Journal of Geophysical Research, 111*, B08305. https://doi.org/10.1029/2005jb004197

Shearer, P. M. (1990). Seismic imaging of upper-mantle structure with new evidence for a 520-km discontinuity. *Nature, 344*, 121-126. https://doi.org/10.1038/344121a0

Shearer, P. M. (1991). Constraints on upper mantle discontinuities from observations of long-period reflected and converted phases. *Journal of Geophysical Research, 96*(B11), 18147-18182. https://doi.org/10.1029/91jb01592

Shearer, P. M. (1996). Transition zone velocity gradients and the 520-km discontinuity. *Journal of Geophysical Research, 101*(B2), 3053-3066. https://doi.org/10.1029/95jb02812

Shearer, P. M., & Flanagan, M. P. (1999). Seismic velocity and density jumps across the 410- and 660-kilometer discontinuities. *Science, 285*(5433), 1545-1548. https://doi.org/10.1126/science.285.5433.1545

Shearer, P. M., Flanagan, M. P., & Hedlin, M. A. H. (1999). Experiments in migration processing of SS precursor data to image upper mantle discontinuity structure. *Journal of Geophysical Research: Solid Earth, 104*(B4), 7229-7242. https://doi.org/10.1029/1998JB900119

Stixrude, L. (1997). Structure and sharpness of phase transitions and mantle discontinuities. *Journal of Geophysical Research: Solid Earth, 102*(B7), 14835-14852. https://doi.org/10.1029/97JB00550

Stixrude, L., & Lithgow-Bertelloni, C. (2005). Thermodynamics of mantle minerals – I. Physical properties. *Geophysical Journal International, 162*(2), 610-632. https://doi.org/10.1111/j.1365-246X.2005.02642.x

Stixrude, L., & Lithgow-Bertelloni, C. (2011). Thermodynamics of mantle minerals – II. Phase equilibria. *Geophysical Journal International, 184*(3), 1180-1213. https://doi.org/10.1111/j.1365-246X.2010.04890.x

Tauzin, B., Kim, S., & Kennett, B. L. N. (2017). Pervasive seismic low-velocity zones within stagnant plates in the mantle transition zone: Thermal or compositional origin? *Earth and Planetary Science Letters, 477*, 1-13.

Thomas, C., & Billen, M. I. (2009). Mantle transition zone structure along a profile in the SW Pacific: thermal and compositional variations. *Geophysical Journal International, 176*(1), 113-125. https://doi.org/10.1111/j.1365-246X.2008.03934.x

Tsujino, N., Yoshino, T., Yamazaki, D., Sakurai, M., Sun, W., Xu, F., et al. (2019). Phase transition of wadsleyite-ringwoodite in the Mg2SiO4-Fe2SiO4 system. *American Mineralogist, 104*(4), 588-594. https://doi.org/10.2138/am-2019-6823

Turunen, S. T., Luttinen, A. V., Heinonen, J. S., & Jamal, D. L. (2019). Luenha picrites, Central Mozambique – Messengers from a mantle plume source of Karoo continental flood basalts? *Lithos, 346-347*, 105152. https://doi.org/10.1016/j.lithos.2019.105152

VanDecar, J. C., James, D. E., & Assumpção, M. (1995). Seismic evidence for a fossil mantle plume beneath South America and implications for plate driving forces. *Nature, 378*(6552), 25-31. https://doi.org/10.1038/378025a0

Walter, M. J., Kohn, S. C., Araujo, D., Bulanova, G. P., Smith, C. B., Gaillou, E., et al. (2011). Deep mantle cycling of oceanic crust: Evidence from diamonds and their mineral inclusions. *Science, 334*(6052), 54-57. https://doi.org/10.1126/science.1209300

Wei, S. S., & Shearer, P. M. (2017). A sporadic low-velocity layer atop the 410 km discontinuity beneath the Pacific Ocean. *Journal of Geophysical Research: Solid Earth, 122*(7), 5144-5159. https://doi.org/10.1002/2017JB014100

Wessel, P., Luis, J. F., Uieda, L., Scharroo, R., Wobbe, F., Smith, W. H. F., & Tian, D. (2019). The Generic Mapping Tools version 6. *Geochemistry Geophysics Geosystems, 20*, 5556-5564. https://doi.org/10.1029/2019GC008515

Wood, B. J. (1995). The effect of H2O on the 410-kilometer seismic discontinuity. *Science, 268*, 74. https://doi.org/10.1126/science.268.5207.74

Xu, W., Lithgow-Bertelloni, C., Stixrude, L., & Ritsema, J. (2008). The effect of bulk composition and temperature on mantle seismic structure. *Earth and Planetary Science Letters, 275*(1), 70-79. https://doi.org/10.1016/j.epsl.2008.08.012

Figures

Fig. 1 Previous observations of (a) the 520-km discontinuity and (b) the 560-km discontinuity. The reference IDs are listed in Table S1. The blue polygons in (a) outline the large regions of the 520-km discontinuity observed by Flanagan and Shearer (1998) and Deuss and Woodhouse (2001). Studies that reported a 520-km discontinuity from a global or continent-scale average without geographic locations are not shown here but are listed in Table S2. Red curves are plate boundaries (Bird, 2003).

Fig. 2 (a) Ray paths of SS (reflected at the surface) and its precursors S*d*S (underside reflections off the *d*-km discontinuity). The 410- and 660-km discontinuities are shown in gray, whereas the 520-km discontinuity is in red. (b) Geographic distribution of earthquakes (blue circles) and broadband seismic stations (black triangles) used in this study. (c) Data coverage of SS bounce points of 139,807 records in the source-receiver distance range of 110°–145° used in this study. Circles are color-coded by the number of stacked seismic records. Note that each cap is larger than the circle shown on the map. Red curves are plate boundaries (Bird, 2003).

Fig. 3 Transverse-component seismograms of the entire dataset (264,625 SS records) stacked in bins of source-receiver distance. Records are aligned and stacked along the SS peak amplitude. Positive amplitudes are in red and negative in blue. Black curves are predicted traveltimes for SS, S*d*S, and other possible interfering phases, with the source at 35-km depth. The dashed box marks the source-receiver distance range (110°–145°) used in this study. The curve at the top shows the number of records in each source-receiver distance bin.

Fig. 4 Examples of stacked S*d*S waveforms in overlapping bouncepoint caps with 10° radius. (a) Geographic locations of caps #0149, #0554, #0765, and #1172 (dots), and profile AA' (black curve). Dashed contours mark areas of the 10° caps. Red curves are plate boundaries (Bird, 2003). (b) Stacked S*d*S waveforms for cap #0149, which has a single S*520*S peak. The three traces from bottom to top are observed, synthetic and residual S*d*S waveforms, respectively. The gray dashed curves are the 95% confidence levels of the stacked waveforms. The amplitudes of the residual S*d*S waveform are scaled up by 2 for better visualization. The two black vertical lines mark the time window for detecting potential S*d*S signals. (c) Same as (b), except for cap #0554, which has both S*520*S and S*560*S signals. (d) Stacked S*d*S waveforms along profile AA' across the North Pacific Ocean. Observed, synthetic, and residual S*d*S waveforms are shown from left to right, respectively.

Fig. 5 (a) Detection of the 520-km discontinuity in overlapping bouncepoint caps with 10° radius. A high S*520*S/S*410*S amplitude ratio suggests a confident detection. Caps with less than 200 traces or stacking uncertainties larger than 0.004 are skipped. Note that each cap is larger than the circle shown on the map. Red curves are plate boundaries (Bird, 2003). (b) Histogram for S*520*S/S*410*S amplitude ratios, with the mean and standard deviation shown at the top right corner. (c) Detection of the 560-km discontinuity. White circles indicate no 560-km discontinuity is detected even though the data sampling is sufficient. (d) Histogram for S*560*S/S*410*S amplitude ratios, with the mean and standard deviation shown at the top right corner.

Fig. 6 Histograms showing apparent depths of the 410-, 520-, 560- and 660-km discontinuities, with their peak-to-peak depth ranges indicated above. The mean depth uncertainties are ~2.5 km for the 410- and 660-km discontinuities and ~9 km for the 520- and 560-km discontinuities (Fig. S6). For the 520- and 560-km discontinuities, only data with depth uncertainties smaller than 10 km are shown. Note that the apparent depths are not corrected for 3-D shear-wave velocity above 410-km depth or for surface topography. Therefore, the actual depth variations should be smaller than the values in the figure, and there should be a distinct depth separation between the 520- and 560-km discontinuities.

Fig. 7 (a-f) Geographic distribution of different depths (a) *d*520-*d*410, (b) *d*560-*d*410, (c) *d*660-*d*520, (d) *d*660-*d*560, (e) *d*660-*d*410, and (f) *d*560-*d*520. Note that the color scale in (a) is reversed compared to others. (g-l) Correlation between differential depths and average shear-wave velocity perturbations between the two depths based on the S40RTS model (Ritsema et al., 2011). The correlation coefficients (CCs) are also shown.

Fig. 8 Stacked SS and S*d*S waveforms processed by different filters in a bouncepoint cap beneath the Coral Sea northeast of Australia (cap #1172 in Fig. 4a). We use a bandpass filter of (a) 15–60 s, (b) 15–75 s (used for the final results), (c) 15–100 s, and (d) 25–75 s. For S*d*S waveforms, observed, synthetic, and residual waveforms are shown from bottom to top. The amplitudes of residual S*d*S waveforms are scaled up by 2 for better visualization.

Fig. 9 Seismic waveform modeling of S*d*S waveforms. (a) Shear-wave velocity and density profiles of the AK135 model (Kennett et al., 1995) (gray lines), pyrolite (Xu et al., 2008) along an adiabat with the potential temperature T_P = 1600 K from equilibrium thermodynamic simulations (orange lines), a successful attempted model with 520- and 560-km discontinuities (black lines) and a failed attempted model with a 60-km-thick 560-km discontinuity (red lines). (b) Comparisons of the reference S*d*S waveform (blue) and synthetic seismograms for models shown in (a). The parameters of attempted models are shown on top of each waveform, with *d*Imp and *d*H denoting the impedance contrast and thickness of the discontinuities. Note that the depths and contrasts of the 410- and 660-km discontinuities in the attempted models are fixed to the values of the AK135 model, thus the arrival times and amplitudes of S*410*S and S*660*S signals do not exactly match the observations.

Fig. 10 (a) Shear-wave velocity and (b) density contrasts (black lines, arrows and numbers) caused by the phase transition of wadsleyite (Wd) to ringwoodite (Rw) near 520-km depth and the exsolution of Ca-perovskite (Ca-pv) from majorite garnet (Mj) near 560-km depth along an adiabat with the potential temperature T_P = 1600 K. Seismic profiles for 7 mol%, 13 mol%, and 20 mol% Ca-perovskite are shown as solid, dashed and dotted lines, respectively. Seismic profiles of pyrolite (Xu et al., 2008) along an adiabat with T_P = 1600 K from equilibrium thermodynamic simulations are shown in orange. The AK135 model (Kennett et al., 1995) is shown in gray.

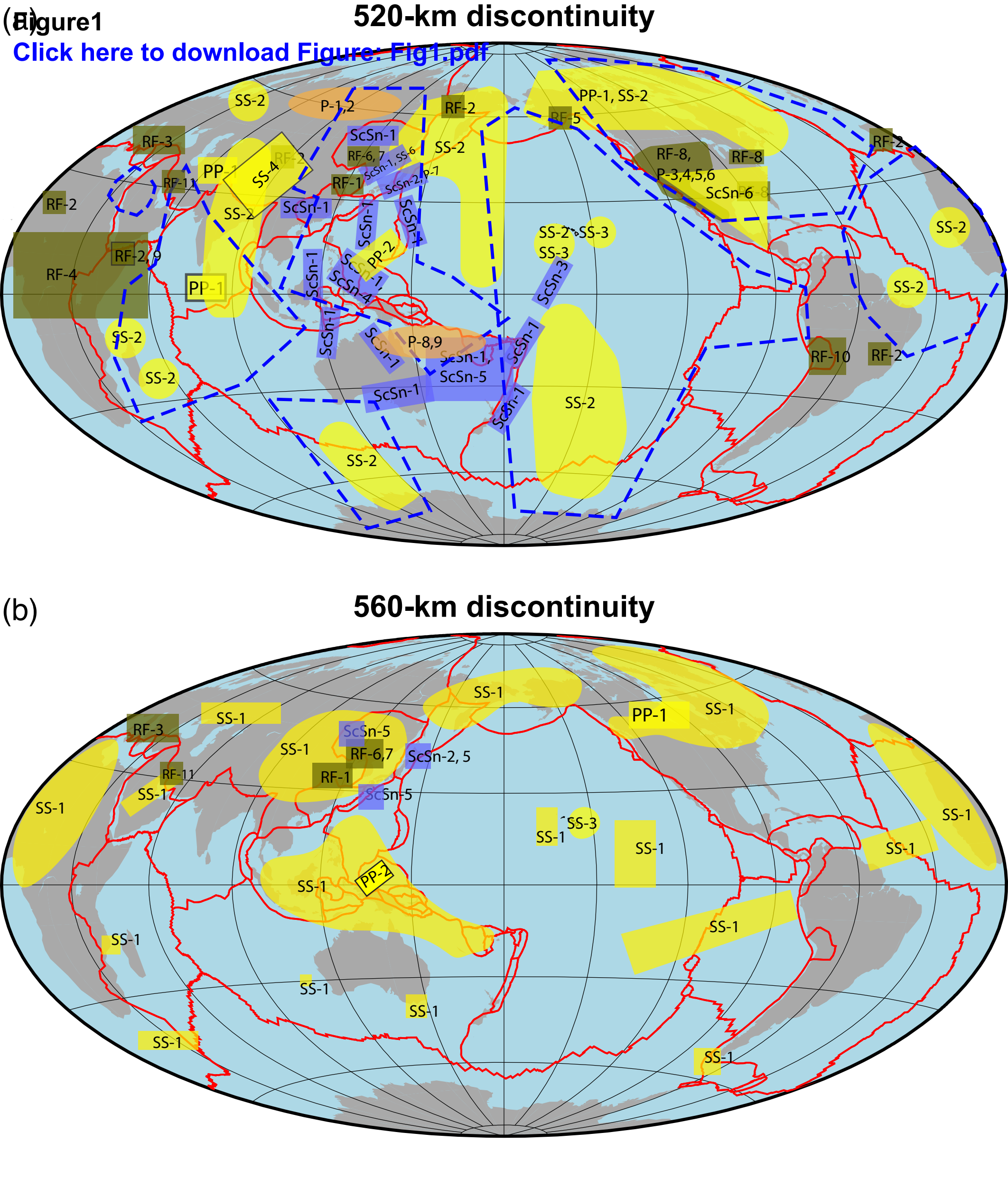
(a)
520-km discontinuity
SS-2
P-1,2
RF-2
PP-1, SS-2
RF-5
RF-3
ScSn-1
SS-4
RF-2
RF-6, 7
ScSn-1, SS-6
ScSn-2, P-1
PP-1
RF-11
RF-1
RF-8,
P-3,4,5,6
RF-8
ScSn-6
RF-2
ScSn-1
SS-2
RF-4
RF-2, 9
PP-1
PP-2
SS-2 SS-3
SS-3
ScSn-3
ScSn-4
P-8,9
ScSn-1,
ScSn-5
RF-10
RF-2
ScSn-1
(b)
560-km discontinuity
SS-1
PP-1
RF-3
ScSn-5
RF-6,7
ScSn-2, 5
RF-1
RF-11
ScSn-5
SS-3
PP-2

Figure2

Click here to download Figure: Fig2.pdf

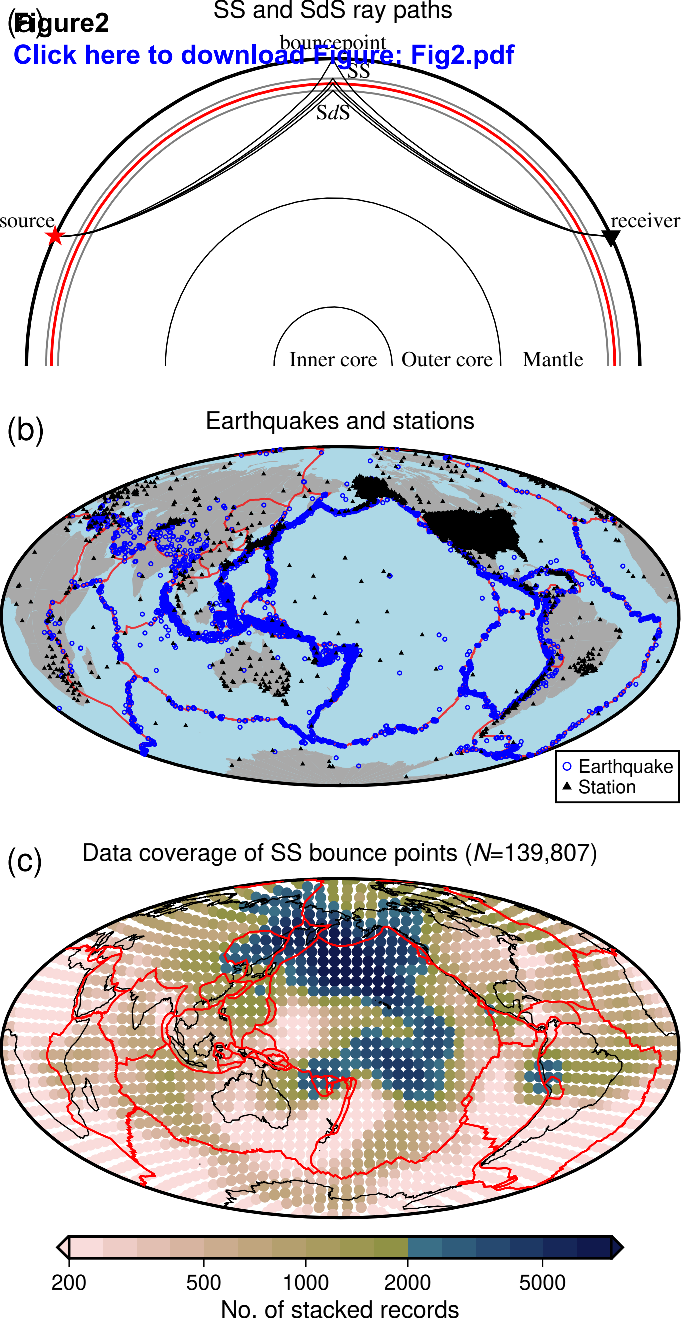

Figure3

Click here to download Figure: Fig3.pdf

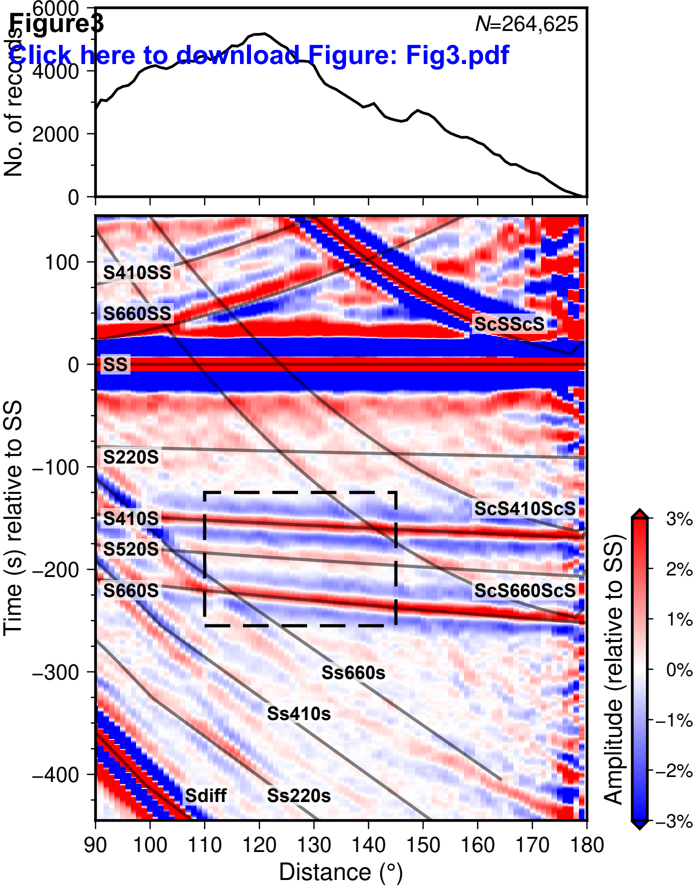

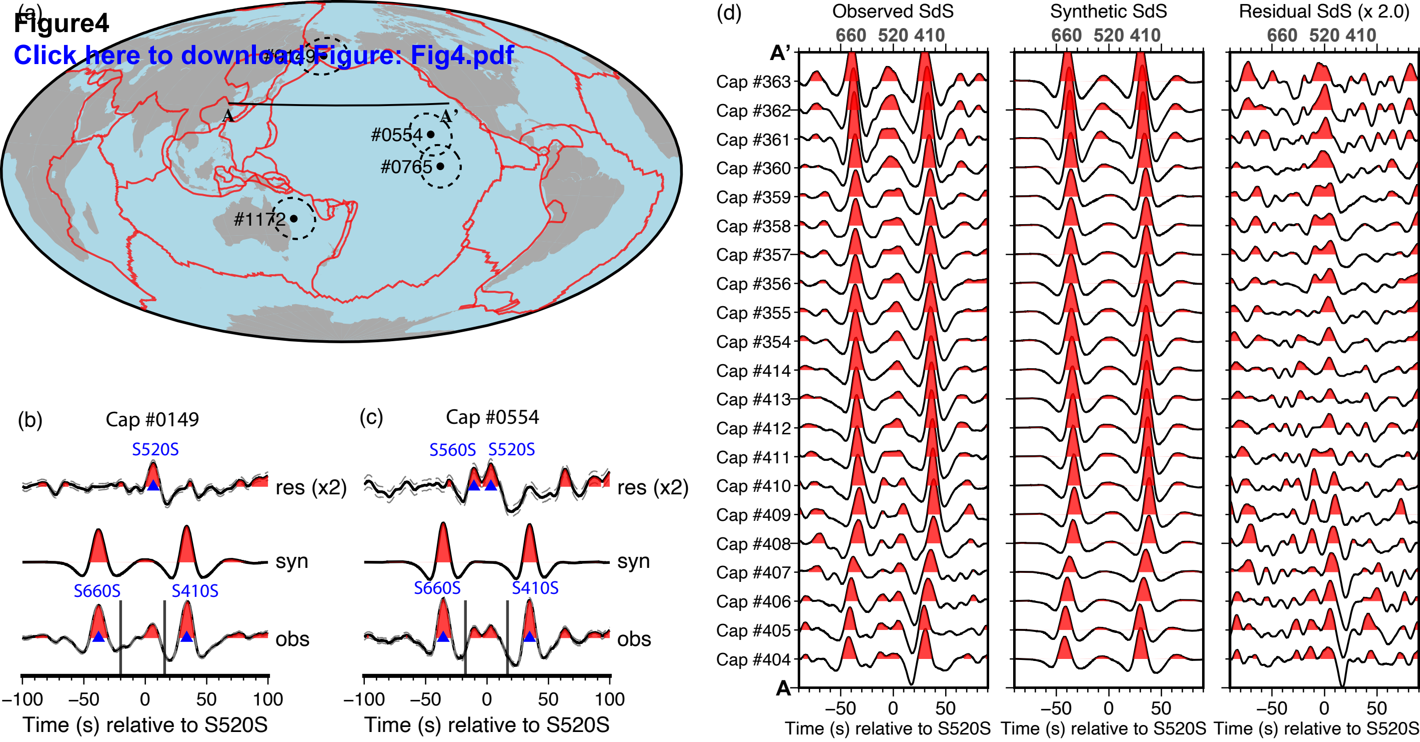
(a)
#0149
A
A'
#0554
#0765
#1172
(b)
Cap #0149
S520S
res (x2)
syn
S660S
S410S
obs
−100
−50
0
50
100
Time (s) relative to S520S
(c)
Cap #0554
S560S
S520S
res (x2)
syn
S660S
S410S
obs
Time (s) relative to S520S
(d)
Observed SdS
Synthetic SdS
Residual SdS (x 2.0)
660 520 410
A'
Cap #363
Cap #362
Cap #361
Cap #360
Cap #359
Cap #358
Cap #357
Cap #356
Cap #355
Cap #354
Cap #414
Cap #413
Cap #412
Cap #411
Cap #410
Cap #409
Cap #408
Cap #407
Cap #406
Cap #405
Cap #404
A
−50
0
50
Time (s) relative to S520S

Figure5

Click here to download Figure: Fig5.pdf

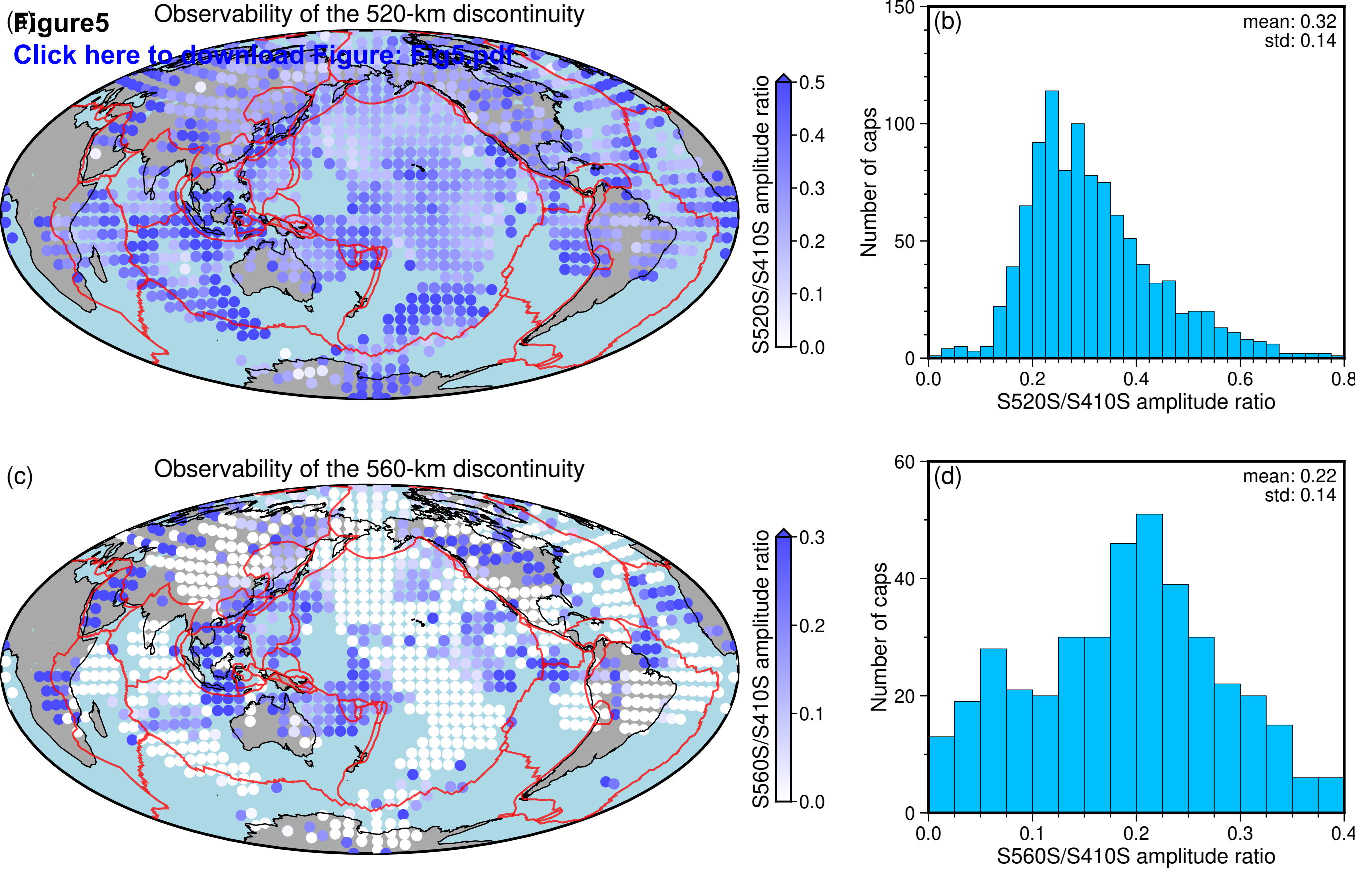

Figure6

Click here to download Figure: Fig6.pdf

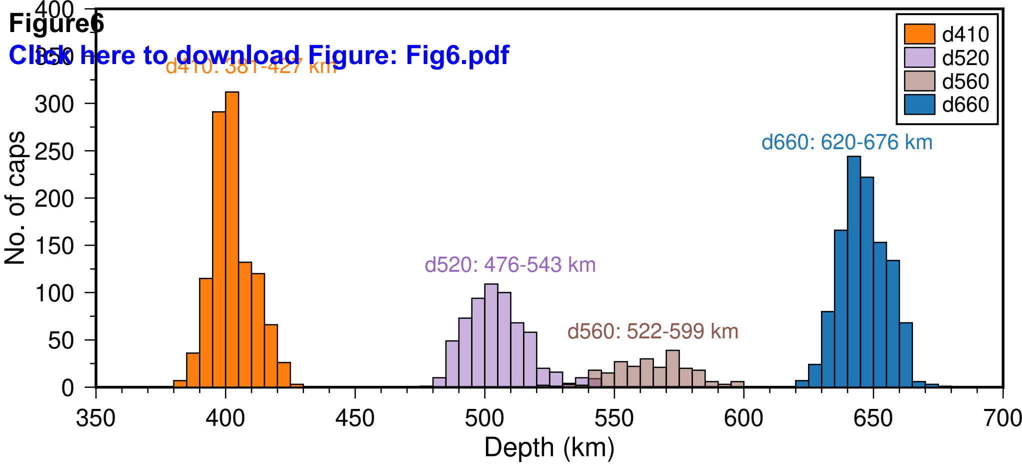

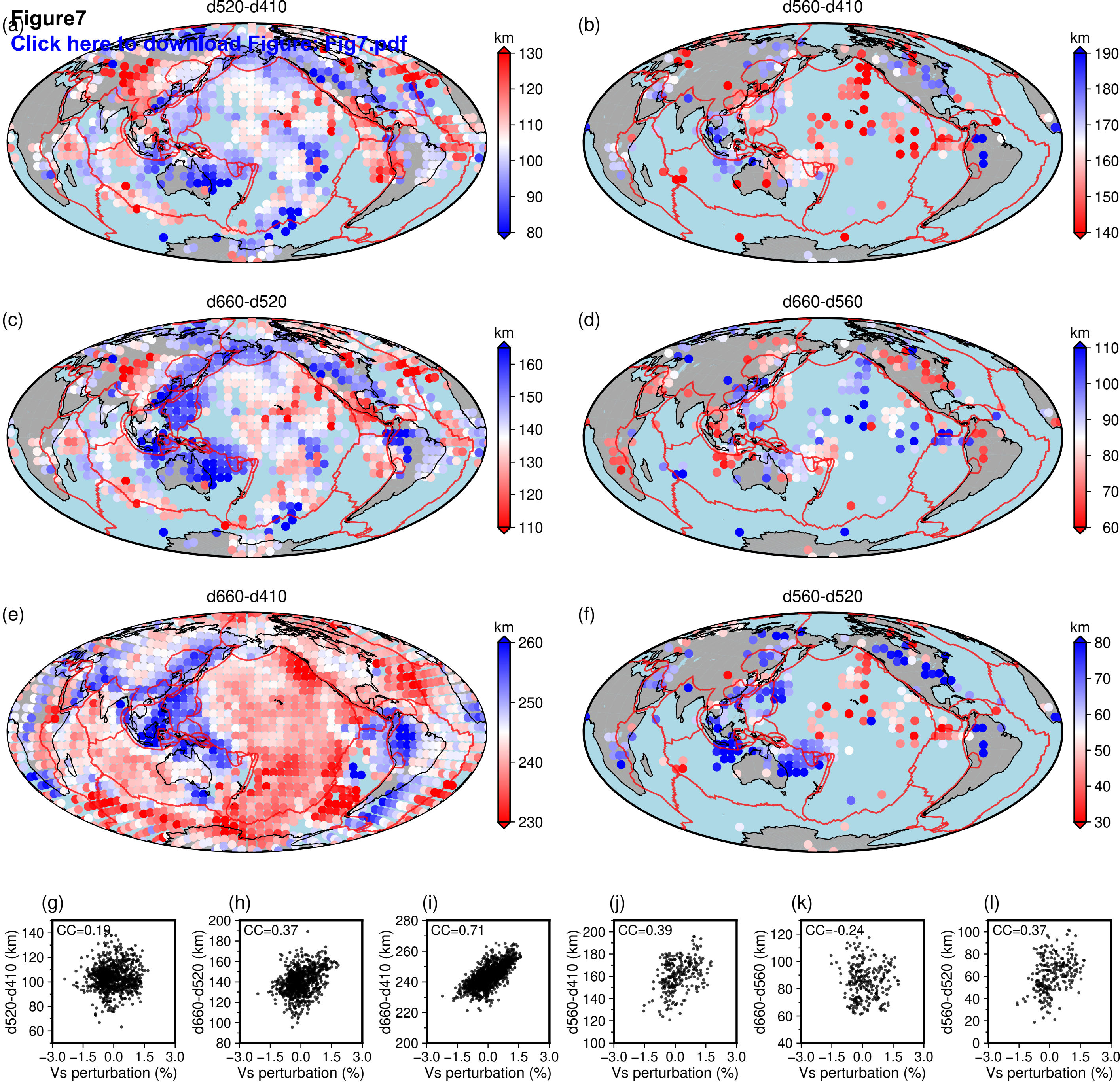
(a)
d520-d410
km
130
120
110
100
90
80
(b)
d560-d410
km
190
180
170
160
150
140
(c)
d660-d520
km
160
150
140
130
120
110
(d)
d660-d560
km
110
100
90
80
70
60
(e)
d660-d410
km
260
250
240
230
(f)
d560-d520
km
80
70
60
50
40
30
(g)
CC=0.19
d520-d410 (km)
Vs perturbation (%)
(h)
CC=0.37
d660-d520 (km)
Vs perturbation (%)
(i)
CC=0.71
d660-d410 (km)
Vs perturbation (%)
(j)
CC=0.39
d560-d410 (km)
Vs perturbation (%)
(k)
CC=-0.24
d660-d560 (km)
Vs perturbation (%)
(l)
CC=0.37
d560-d520 (km)
Vs perturbation (%)
−3.0 −1.5 0.0 1.5 3.0

Figure8

Click here to download Figure: Fig8.pdf

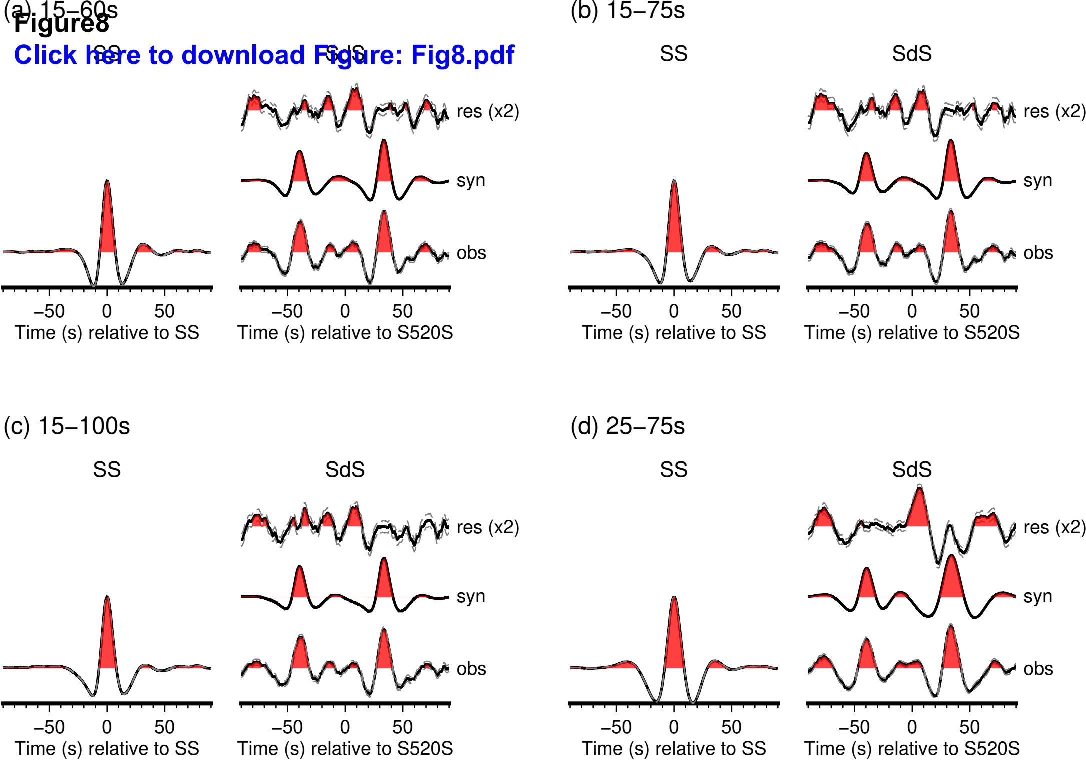

Figure9

Click here to download Figure: Fig9.pdf

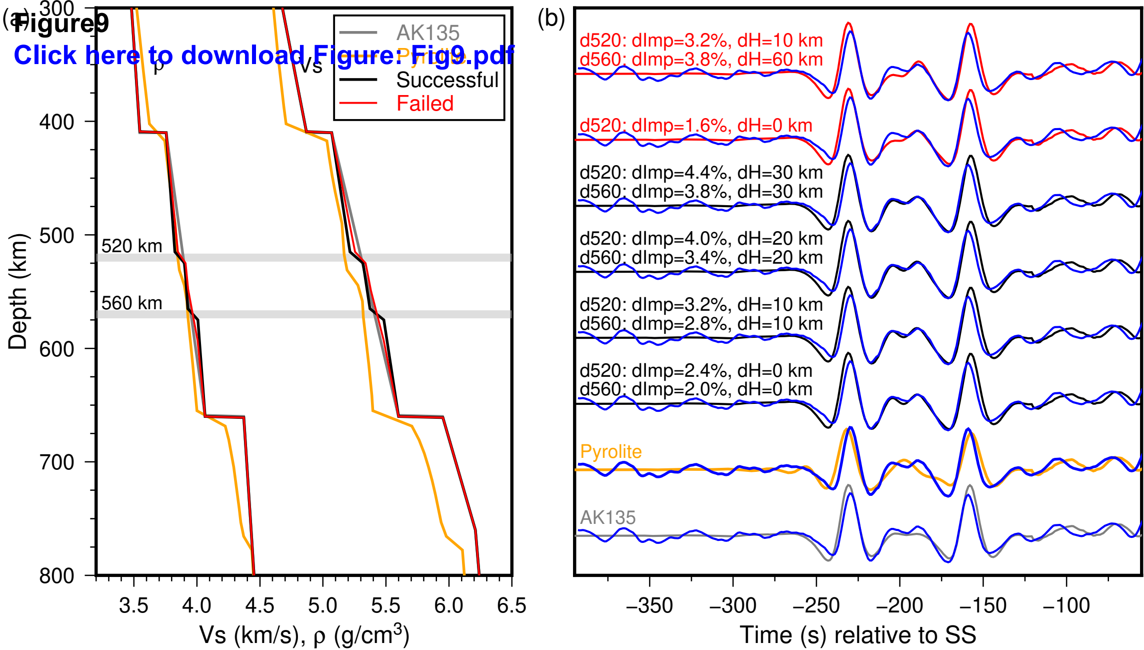

Figure10

Click here to download Figure: Fig10.pdf

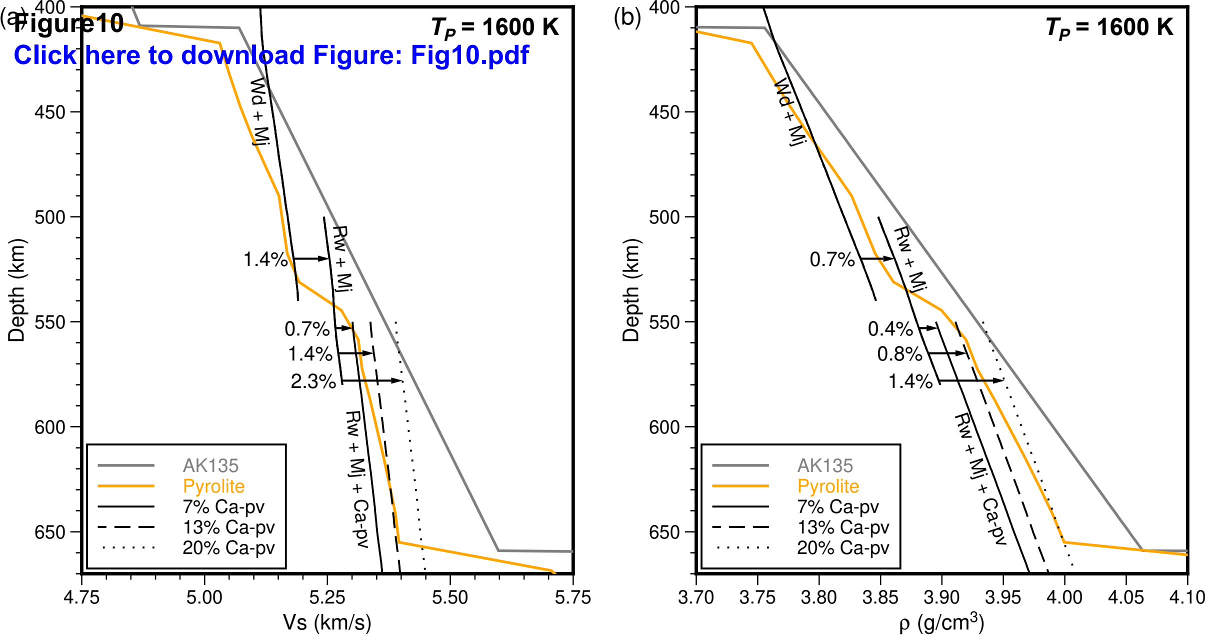

***Declaration of Interest Statement**

Declaration of interests

☒ The authors declare that they have no known competing financial interests or personal relationships that could have appeared to influence the work reported in this paper.

☐The authors declare the following financial interests/personal relationships which may be considered as potential competing interests:

CRediT Author Statement

Dongdong Tian: Conceptualization, Methodology, Formal analysis, Data Curation, Investigation, Visualization, Writing - Original Draft, Writing - Review & Editing

Mingda Lv: Methodology, Validation, Writing - Review & Editing

S. Shawn Wei: Conceptualization, Methodology, Formal analysis, Writing - Review & Editing, Supervision, Project administration, Funding acquisition

Susannah M. Dorfman: Writing - Review & Editing, Funding acquisition

Peter M. Shearer: Writing - Review & Editing, Funding acquisition